UPCommons

Portal del coneixement obert de la UPC

http://upcommons.upc.edu/e-prints

Onset of temporal dynamics within a low Reynolds-number laminar fluidic oscillator

Wasim Sarwar[a,*], Josep M. Bergadà[b], Fernando Mellibovsky[a]

[a]*Department of Physics, Aerospace Engineering Division, Universitat Politècnica de Catalunya, 08034, Barcelona*
[b]*Department of Fluid Mechanics, Universitat Politècnica de Catalunya, Barcelona-Tech 08034, Spain*

Abstract

We investigate the onset of temporal dynamics of a fluidic oscillator (FO) in the laminar regime at very low Reynolds number ($Re = Uh_i/\nu$, where U and h_i are the velocity and channel height at inlet, and ν is the kinematic viscosity of the fluid). Both two- and spanwise-periodic-three-dimensional simulations are performed using high-order spectral element methods to characterise the flow inside the FO cavity and the outcoming jet. While the flow remains steady and symmetric for sufficiently low Re, the two-dimensional FO undergoes a symmetry-breaking Hopf bifurcation at $Re_{H_2} = 75.7$ that results in a space-time symmetric periodic solution. The remnant space-time symmetry is later broken in a pitchfork bifurcation of limit cycles at $Re_{P_2} = 294.2$. Taking three-dimensionality into consideration results in an early spanwise-invariance disruption at about $Re_3 \simeq 68$ of wavelength $13h_i$ that retards the onset of the oscillation to $Re_{H_3} = 82.1$. This effect is little representative of actual FO implementations, which are typically much narrower than the wavelength of the spanwise instability observed at these low Re. Contrary to what happens with FOs in the turbulent oscillatory regime, the oscillation frequency of the output jet in the laminar regime is found to decrease with Re. The mechanism that drives the oscillation, however, remains the same: as the high speed flow inside the cavity attaches to one of the internal walls through the Coandă effect, the feedback channels divert part of the momentum back, which pushes the incoming flow against the opposite wall. The alternate deviation of the flow inside the cavity to one or the other side results in the periodic flipping of the output jet. The pressure contribution to net momentum at the end of the feedback channels is found to be double that of the advective momentum flux at the early time-periodic regime but both become comparable as Re is increased. The jet sweeping angle amplitude is more pronounced for the two-dimensional FO as compared to three-dimensional at a fixed given Re, the Coandă effect being only partially fulfilled in the latter case. In both cases the sweep amplitude increases with Re. The instability of the output jet, which becomes slightly chaotic already at very low Re, is responsible for triggering the cavity instability that drives the oscillation slightly earlier than it would, should outside noise be suppressed altogether.

Keywords: Fluidic oscillator; transitional flow; oscillating jet;

1. Introduction

Fluidic oscillators (FO) are devices that produce a periodically-oscillating jet at output provided a steady supply of pressurised fluid is available on input [1, 2]. The characteristic sweeping motion of the emanating jet is self-induced and self-sustained due to inherent flow instabilities. Fluidic oscillators might be feedback-free and thus rely on a Kelvin-Helmholtz-type instability, or employ feedback channels to alternatively exploit and suppress the Coandă effect [3, 4, 5]. Both types may exhibit a wide range of oscillation frequencies and sweeping angle amplitudes depending on geometrical parameters, and are commonly used in engineering

---

*Corresponding author
Email address: wasim.sarwar@upc.edu (Wasim Sarwar)

applications such as flow separation control [6, 7], drag reduction [8], combustion control [9], mixing and heat transfer enhancement [10, 11, 12, 13, 14], jet thrust vectoring [15], etc.

Sweeping-jet oscillators are often classified into two groups, i.e. jet-interaction and wall-attachment fluidic oscillators, based on the mechanisms that drive the oscillation. The standard design of jet-interaction-type fluidic oscillators involves two separate and constant input flow streams that enter the plenum chamber, typically in a symmetric fashion. The chamber is designed such that the mixing of the two streams triggers a shear instability which generates a self-induced and self-sustained time-periodic jet on output. In an experimental investigation using pressure sensitive paint (PSP), Gregory et al. [16] observed that the interaction of the incoming power streams within the mixing/interaction chamber results in the formation of a Kelvin-Helmholtz-unstable shear layer. The ensuing complex interaction of counter-rotating vortices that form at either side of the shear layer is then exploited to generate a sweeping jet at the exit of the device. Gregory et al. [17] studied a jet-interaction micro fluidic oscillator in order to characterise the relation between power supply rate and output oscillation frequency from the standpoint of potential applications. The irregular trends they observed, including a change of slope, seemed to indicate that distinct driving mechanisms might be at play depending on the flow regime considered. As a matter of fact, three different jet oscillation types were later revealed using particle image velocimetry (PIV) with a refractive-index-matched sodium-iodide solution [18]. The corresponding flow regimes were named *weak* (or *low*), *transitional* and *high* flow-rate regimes. A detailed analysis in the *weak* regime showed that the transfer of kinetic energy between the interacting streams is regulated by the redirection of part of the outcoming jet towards either side of the cavity dome [see Table 1 in 19]. Phase averaging unveiled the presence of four vortices, two dome and two side vortices. The former, which appear and disappear alternatively along a full cycle, were shown responsible for the splitting of the jet, while the latter, present all along, alternatively grew and shrank thus regulating the exit jet oscillatory properties [19].

Wall-attachment-type fluidic oscillators base their operation instead on the alternate attachment of a single input flow stream, fed through the so-called power nozzle, unto one or the other of the internal walls of the mixing/plenum chamber through the Coandă effect. The underlying mechanism relies on the bi-stability of two mutually-symmetric wall-attached (to either one of the two walls) flow configurations (or states) that are alternatively destabilised by the timely diversion of momentum through purposely-designed feedback channels that push the flow stream towards the opposite wall. The alternate bending of the stream as it wanders from one wall to the other results in the sweeping motion of the outcoming jet beyond the exit nozzle. Before the introduction of feedback channels, the switching mechanism of the power stream between the adjacent walls was driven by the application of a transverse disturbance in the form of a pressure pulse [20] or a fluid injection [21], such that the oscillation would not qualify as self-sustained. Nowadays, a typical curved-sweeping-jet oscillator replaces the external momentum source as switching mechanism by an adequate diversion of ouput momentum through purposefully designed feedback channels. The power stream, attached to either one of the side walls by the action of the Coandă effect, is made to impinge quasi-orthogonally on the wall that leads to the exit nozzle throat. As a result, part of the momentum is directed towards the feedback channel on the side to which the stream is bent. This momentum is reintroduced back transversally at the exit of the power nozzle, which pushes the power stream away from the wall to which it is attached. As the power stream dettaches from the wall, a recirculation bubble grows that blocks the inlet to the feedback channel. Once the recirculation bubble has grown sufficiently large, the feedback source of pushing momentum is cut but the power stream has already been left at the mercy of the Coandă effect from the opposite wall, which captures it, thus completing the full sweep of the jet [22]. The process then repeats symmetrically. The alternate sweeping of the power stream leads to a self-induced and self-sustained oscillating jet at exit [23] in complete absence of moving parts, which renders these devices very robust and reliable against mechanical failure. Mass injection has been long thought the main source of feedback momentum that drives the jet sweeping for these type of devices, as time resolved pressure and PIV measurements [22] seem to reflect. Baghaei and Bergada [24] have nevertheless shown that static pressure may become the main feedback momentum source underlying the sweeping mechanism under certain circumstances.

In the present work, the focus has been placed on the detailed investigation of low Reynolds number flow dynamics inside a laminar fluidic oscillator as well as on ellucidating the mechanisms underlying the onset
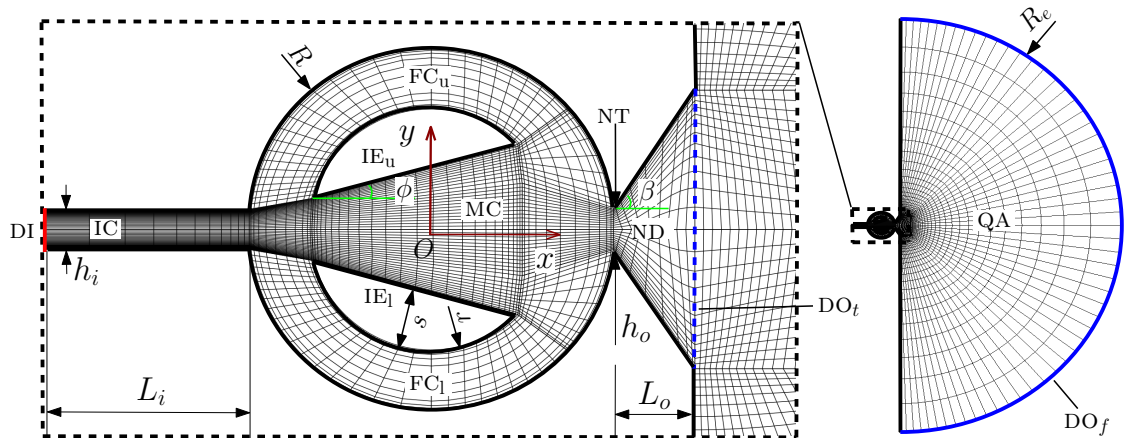
Fig. 1: Computational domain and mesh. Domain and FO geometry dimensions are duely annotated. The inset shows a detail of the mesh inside the fluidic oscillator. The streamwise-crossflow plane is discretised with high-order quadrilateral spectral elements. The acronyms denote inlet channel (IC), plenum or mixing chamber (MC), upper and lower internal elements (IE$_{u,l}$) and feedback channels (FC$_{u,l}$), nozzle throat (NT) and divergent section (ND), and quiescent atmosphere (QA). The boundaries are labelled DI (domain inlet, red), DO$_{f,t}$ (domain outlet, blue, continuous for full domain, dashed for truncated domain), and NW (no-slip walls, black).

of time-dependence and the subsequent transitions in the framework of bifurcation theory. Linear stability theory has been employed to investigate the three-dimensionalisation of the flow through the characterisation, in terms of growth rate and spatial structure, of the spanwise-dependent leading eigenmodes.

The paper is structured as follows. §2 outlines the governing equations together with the numerical methods adopted for time integration. In §3 the dynamical properties of the flow are clarified by suitable phase-space projections of flow parameters at varying Reynolds number. §4 is devoted to the linear stability analysis of the two-dimensional time-dependent flow inside the FO to three-dimensional perturbations, at Reynolds numbers encompassing the entire flow regime under scrutiny. The physical mechanisms underlying the early flow transitions undergone by the flow inside the FO at low Re are explained in §5. The main findings and conclusions are finally summarised in §7.

2. Problem formulation and numerical approach

The incompressible Newtonian flow inside a fluidic oscillator is governed by the Navier-Stokes equations, which, after suitable nondimensionalisation with inlet width h_i and upstream mean flow velocity U, read

$$\begin{aligned} \frac{\partial \mathbf{u}}{\partial t} + (\mathbf{u} \cdot \nabla)\mathbf{u} &= -\nabla p + \frac{1}{Re}\nabla^2 \mathbf{u}, \\ \nabla \cdot \mathbf{u} &= 0, \end{aligned} \tag{1}$$

where $\mathbf{u}(\mathbf{r};t) = (u,v,w)$ and $p(\mathbf{r};t)$ are the nondimensional velocity and pressure, respectively, at nondimensional time t and location $\mathbf{r} = (x,y,z)$, with x, y and z the streamwise, crossflow and spanwise coordinates, and u, v, and w the velocity components along the x, y and z directions, respectively. $Re = Uh_i/\nu$ is the Reynolds number, with ν the kinematic viscosity of the fluid. The laminar plane-Poiseuille velocity profile $\mathbf{u} = u(y)\mathbf{i} = 3(1-y^2)/2$, of unit average, has been prescribed at the inlet channel.

The FO geometry is shown and annotated in Fig. 1 alongside the full computational domain. The coordinate origin (O) has been placed at the centre of the circular FO cavity. Following the nondimentionalisation, the inlet nozzle width is $h_i = 1$. The nozzle throat width has been set equal to that of the inlet at $h_n = h_i = 1$. The outer radius of the circular cavity of the FO is $R = 4.5$. A minimum inlet channel length of $L_i = 5$ has been adopted to avoid an impact of inlet boundary conditions on the internal dynamics of

3

Table 1: Mesh and aerodynamics parameters of fluidic oscillator

Re	K	P	St	$\bar{C}_L$	C'_L	$\bar{C}_D$	C'_D
100	4694	4	0.01284	-0.8540	0.5327	0.0843	0.0728
-	4694	6	0.01282	-0.8585	0.5374	0.0852	0.0734
-	4694	8	0.01279	-0.8586	0.5378	0.0851	0.0736
-	6476	4	0.01286	-0.8559	0.5334	0.0842	0.0726
-	6476	6	0.01281	-0.8599	0.5385	0.0848	0.0733
300	4694	4	0.00822	-2.0488	1.7205	0.5649	0.4116
-	4694	6	0.00823	-2.0470	1.7263	0.5665	0.4142
-	4694	8	0.00826	-2.0468	1.7271	0.5675	0.4153
-	6476	4	0.00823	-2.0472	1.7238	0.5651	0.4139
-	6476	6	0.00831	-2.0469	1.7275	0.5685	0.4161

the FO. Also to avoid artificially affecting the internal flow dynamics, the outlet boundary conditions have been pushed away into the quiescent atmosphere, leaving a semi-circular external domain of radius $R_e = 75$. The internal elements are circular segments of radius $r = 3$, centre at the origin O, and sagitta $s = 1.5$, symmetrically mounted within the FO cavity with tilt $\phi = \pm\pi/12$. The divergent exit nozzle semi-angle is taken as $\beta = 14\pi/45$ and its length is $L_o = 2$.

The boundary conditions for velocity are Dirichlet at inlet (the parabolic profile), Dirichlet homogeneous ($\mathbf{u}_w = 0$, non-slip) at all walls and homogeneous Neumann ($\nabla \mathbf{u} \cdot \hat{\mathbf{n}} = 0$) at the downstream boundary. For pressure, high-order homogeneous Neumann boundary conditions are applied everywhere except for the downstream boundary, where a homogeneous Dirichlet condition ($p = 0$) is enforced.

The equations have been discretised in space on a structured mesh consisting exclusively of quadrilateral (QUAD) elements using the incompressible Navier-Stokes solver of the spectral/finite element package Nektar++ [25], enforcing a continuous Galerkin projection across element boundaries. The skew-symmetric form of the advection term has been adopted for the discrete advection operator in order to preserve the symmetry properties of the continuous operator. The spatially discretised system has been evolved in time with a second-order velocity-correction splitting scheme with a time-step $\Delta t = 0.005$, shown to provide adequate time-integration accuracy at $Re = 100$. For $Re = 300$, the time-step has been reduced to $\Delta t = 0.002$.

A two-dimensional resolution study has been performed at both $Re = 100$ and 300 to produce the optimal mesh balancing sufficient accuracy and reasonable requirements in terms of computational resources. Two different in-plane structured quad meshes were built and the elements discretised with varying order polynomial expansions (P) to assess the effects on a collection of global flow parameters, namely the nondimensional jet oscillation frequency (Strouhal number $St \equiv fh_i/U$), and time-averaged and rms lift ($\bar{C}_L$, C'_L) and drag ($\bar{C}_D$, C'_D) force coefficients (defined as $C_x \equiv \frac{F_x}{\frac{1}{2}h_iU^2}$) on the upper internal element, as shown in table 1. A spatial discretisation of $K = 4694$ high-order quadrilateral elements, with Lagrange polynomial expansions of order $P - 1 = 5$, have been deployed in the streamwise-crossflow plane, as all monitored global quantities fall within the 1% tolerance accepted here as sufficiently accurate for the purposes of our study. In order to properly resolve the complex internal dynamics inside the FO, the mesh has been set up particularly fine in the regions where the flow experiences the largest space and time variations, namely within the mixing chamber, the inlet and outlet of the feedback channels, and the outlet nozzle, as shown in Fig. 1. For an accurate description of boundary layers, the quad elements have been set purposefully thin close to the walls, such that the first element away from the wall was always at a distance in wall-units $y^+ \leq 0.27$, well within the viscous sublayer of a hypothetically turbulent boundary layer.

The two-dimensional geometry and structured mesh in Fig. 1 has been employed throughout the paper in order to characterise the initial transitions leading to time-dependent two-dimensional solutions. We denote these simulations on the full two-dimensional domain as F2D. Part of the analysis has been however repeated on a truncated two-dimensional domain by eliminating the semicircular quiescent fluid region
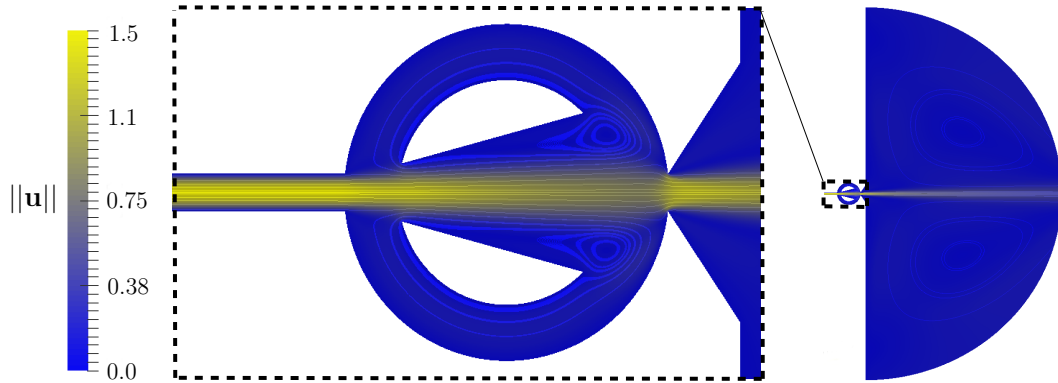
4

Fig. 2: Velocity magnitude $\|\mathbf{u}\|$ colourmap and streamlines at $Re = 75$, $\|\mathbf{u}\| \in [0, 1.5]$. The figure corresponds to F2D, but is identical to that for F3D.

altogether and replacing it by a straight outlet (indicated with a dashed blue line in Fig. 1). A Dirichlet boundary condition enforcing the time-averaged pressure distribution from full domain computations and a homogeneous Neumann boundary condition for velocity have been applied to the truncated outlet, and the simulations on the truncated domain designated as T2D. Finally, a few simulations on a three-dimensional domain with in-plane geometry and mesh coincident with that of F2D, but homogeneously extended in the spanwise direction, have also been run to understand the actual three-dimensional structure of the flow inside the FO and dubbed F3D. The spanwise periodic extent has been set to $L_z = 14$ as suggested by the stability analysis of the underlying two-dimensional flow to three-dimensional perturbations, and discretised using a Fourier expansion with 20 modes, which exhibited a modal energy decay in excess of 6 orders of magnitude at $Re = 88$.

3. Characterisation of FO solution types

At sufficiently low $Re \lesssim 76$, the flow inside the FO is steady and reflectional symmetric. As the Reynolds number is increased beyond a certain threshold, the flow develops into increasingly complex time-dynamics and space topologies following a series of ordinary local bifurcations. We shall see that the transition path starts with the onset of a space-time symmetric periodic oscillation featuring low amplitude chaotic dynamics associated to the downstream farfield instability of the oscillating jet. This rather unusual inception of time-dynamics, including mild chaotic fluctuations, requires using a sufficiently large external region, as is the case for F2D simulations using the full domain. Meanwhile, T2D computations on the truncated domain suppress the jet instability along with the chaotic background noise. Furthermore, F3D simulations on the spanwise-periodic three-dimensional domain show that the first transition does not introduce time-dynamics, but a disruption of the spanwise translational invariance instead, such that three-dimensionality precedes time-dependence. In what follows, we analyse the diverse flow topologies and dynamics and their dependence on the particulars of the domain chosen for the simulations. In particular, we analyse what the origin of the background chaotic noise is and the effects of three-dimensionality on the onset of time-periodicity. The F2D and T2D analyses will be carried further to increasing flow regimes to try and ellucidate the transition route to fully chaotic dynamics.

The base flow, which acts as a global attractor at sufficiently low Reynolds numbers, is a two-dimensional reflectional-symmetric steady-state solution, as clearly exemplified at $Re = 75$ by the velocity magnitude $\|\mathbf{u}\|_2$ colourmap of Fig. 2. The inlet channel (IC) discharges an almost unaltered fully-developed plane-Poiseuille flow into the plenum or mixing chamber (MC), where it flies through the narrow passage left by the upstream edges of the two mutually-symmetric diverters/deflectors (internal elements, IE) directly into the nozzle throat (NT), straight and symmetric, only mildly diffused, and then into the quiescent atmosphere (QA), also undeflected and symmetric, where the jet gradually diffuses. The internal stream
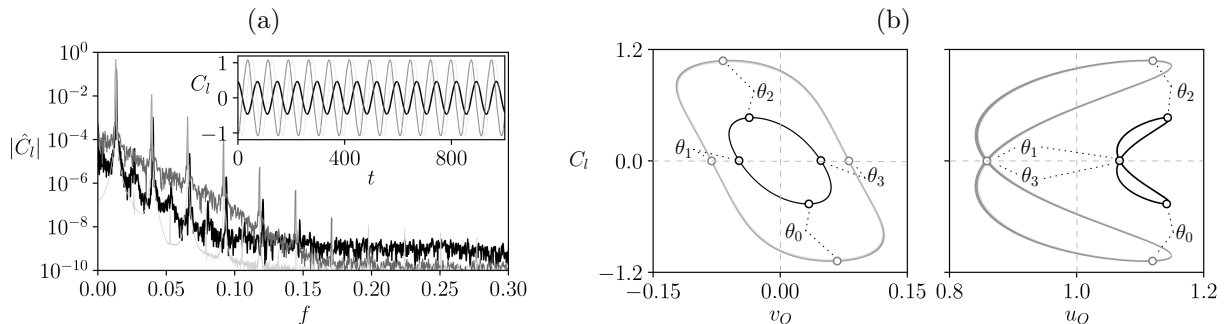
5

Fig. 3: Periodic state for F2D (dark gray line), T2D (light gray) and F3D (black) simulations at $Re = 88$. (a) Spectrum $|\hat{C}_l|$ of the combined lift coefficient signal C_l (shown in the inset) on the upper (ID$_\mathrm{u}$) and lower (ID$_\mathrm{l}$) internal diverters. (b) Phase map projection on the (v_O, C_l) and (u_O, C_l) planes, with (u_O, v_O) the in-plane velocity vector at the origin (O). The instants corresponding to instantaneous phases $\theta_i = \{0, \pi/2, \pi, 3\pi/2\}$ (white circles, $i = \{0, 1, 2, 3\}$) of the analytical signal $C_l^a = C_l + \mathbf{i}\mathcal{H}(C_l)$ ($\mathcal{H}$ denotes the Hilbert transform), are duely marked.

inside the cavity shows no propensity to attach to either one of the circular-segment internal elements, thus leaving two symmetric recirculation bubbles on their respective straight secant sides. At the heart of the recirculation bubbles are two mutually-symmetric counter-rotating stationary vortices trapped between the trailing edge of the IEs and the convergent arc-circular walls of the device cavity leading to the nozzle throat (NT), thus blocking the inlet of momentum into the feedback channels (FC). The internal jet that crosses the plenum is stable enough to remain insensitive to the so-called Coandă effect, which is exerted symmetrically, yet ineffectively, from the straight walls of the diverters. In the open atmosphere (QA), the entrainment effect of the jet results, due to the finite size of the domain, in two very large yet extremely weak counter-rotating vortices that, although unphysical, have no measurable impact on the solution global properties at this low Re or higher.

At slightly higher values of the Reynolds number, solutions are no longer steady and time-dependence has definitely set in. Fig. 3(a) illustrates, at $Re = 88$, the spectrum $|\hat{C}_l|$ of the $C_l(t)$ time series shown in the inset, where C_l is the combined lift coefficient on the upper (ID$_\mathrm{u}$) and lower (ID$_\mathrm{l}$) internal elements. There is a very clear peak at the fundamental frequency $f_0^{\mathrm{F2D}} = 0.0132$ ($\simeq f_0^{\mathrm{T2D}}$), corresponding to a time period $T = 75.76$ for F2D (and T2D), followed by a series of higher-order harmonics at multiples of f_0^{F2D}. The flow state inside the FO is remarkably periodic, and the relatively high energy of the harmonics reveals that it has already evolved non-linearly away from the bifurcation point. A very similar fundamental peak, although shifted to the slightly higher frequency $f_0^{\mathrm{F3D}} = 0.0133$, is obtained for the F3D simulation.

The flow inside the plenum features predominantly periodic oscillations of a space-time symmetric nature. There remains however, for simulations F2D and F3D in the full in-plane domain, a very mild broad-band noise that disrupts the perfect periodicity and space-time symmetry of the signal by evenly distributing power across all frequencies beside the fundamental and harmonics. In the phasemap projections of Fig. 3(b), the background noise widens the sharp lines that would correspond to a perfectly periodic signal into a narrow band that might be transited through all of its width at any given cycle. Phase-map trajectories have been projected onto the (u_O, C_l) and (v_O, C_l) planes for F2D (dark gray), T2D (light gray) and F3D (black) computations at $Re = 88$, where (u_O, v_O) is the in-plane velocity vector in the middle of the plenum at the origin (O). Leaving the effects of the background noise aside, the phase-map trajectories clearly evince the almost perfect space-time symmetry of the solution.

The complete absence of noise for the T2D computation, as ascertained by the low energy levels at all frequencies but the fundamental and harmonics and also by the clear-cut phase-map trajectories, points at an external origin of the chaotic disturbance. Suppressing the farfield instability of the jet by truncating the domain at the nozzle exit and thus eliminating the external region altogether, results in a perfectly periodic and space-time symmetric solution. The background chaotic fluctuations are therefore a result of an instability of the external oscillating jet. The instability inside the FO cavity that triggers the oscillations

6

(a)

θ_0 θ_1 θ_2 θ_3
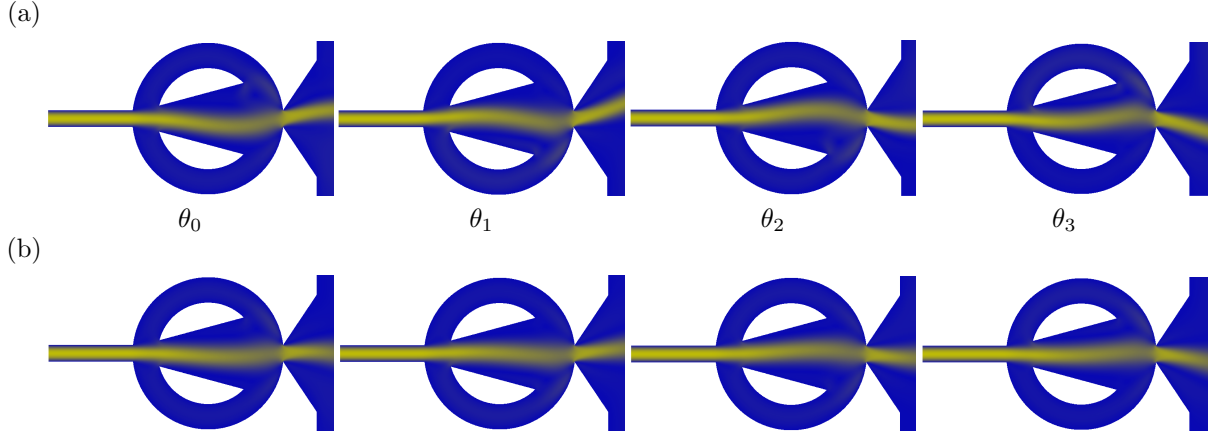
(b)

Fig. 4: Velocity field colourmaps of the periodic solution at $Re = 88$ at instants indicated with white circles in Fig. 3(b) and corresponding to phases $\theta_0, \theta_1, \theta_2$ and θ_3. Simulations on (a) F2D and (b) F3D domains. Colour coding as for Fig. 2.

remains however largely unaffected, as the solution preserves its most salient features both from a qualitative and a quantitative point of view. In this respect, the oscillation must be solely ascribed to an instability of the FO cavity proper and the output jet instability can be discarded as the triggering mechanism.

Four snapshots corresponding to F2D, indicated with white circles in the phase map trajectory of Fig. 3(b), are shown in Fig. 4(a) to illustrate the oscillatory dynamics of the periodic solution at $Re = 88$ along a full cycle. The snapshots have been equispaced along a full period using the instantaneous phase of the analytical signal $C_l^a = C_l + \mathbf{i}\mathcal{H}(C_l)$, where $\mathcal{H}$ denotes the Hilbert transform. The first snapshot, labeled θ_0 depicts the internal/power stream fully attached to ID$_l$. Towards the trailing edge of ID$_l$, the jet bends up and faces the NT with an angle such that the output jet leaving the nozzle into QA points slightly upwards. Part of the momentum is however directed to the inlet of FC$_l$ and effects, when reintroduced through its outlet, the inititation of the dettachment. The stream has been pushed away from ID$_l$ by the time corresponding to the second snapshot, labeled θ_1. The output jet is still bending upwards, even further than before, but the internal stream has already been trapped by the Coandă effect exerted by ID$_u$. The half cycle is completed as the solution attaches completely to the ID$_u$ and reaches the instant captured by the snapshot labeled as θ_2. Half a period has elapsed and the current flow topology is related to the original state by a mere reflection about the midplane. The fourth snapshot, labeled θ_3, is the symmetry conjugate of θ_1, and the cycle resumes its original state as the stream reattaches completely to the ID$_l$ wall.

The effect of taking three-dimensionality into consideration at the same exact Re, as done for F3D simulations, is an attenuation of the oscillation amplitude with respect to the two-dimensional case F2D. This is already visble from the phase-map trajectories of Fig 3(b), but becomes all the more clear upon observation of flowfield snapshots along a full cycle shown in Fig 4(b). While F2D has the power stream fully attached to IE$_l$ at θ_0 through the Coandă effect, which corresponds to maximum downwards deflection, F3D only produces a very mild bending. The result is a much lower amplitude of the output jet deflection angle.

The straight-jet steady-state solution crucially relies on a *spring* force that acts to straighten the power stream back whenever the reflection symmetry is disrupted. The solution remains stable while a sufficient *damping* force exists that prevents the amplification of any deviation from symmetry. Beyond a certain value of the Reynolds number, the damping action becomes ineffective and the steady state is no longer a stable solution. The self-induced and self-sustained oscillation of the resulting sweeping-jet solution critically depends on the existence of the spring force and the absence of sufficient damping. This force is exerted by the FCs by redirecting part of the momentum of the power stream, whenever it is deflected to one side of the MC, into flipping it towards the opposite side. This momentum transfer has two components: advective momentum (inertia force F_i), and pressure momentum (pressure force F_p) fluxes along the FCs, which capture the momentum at MC exit and feed it back transversally at inlet. As the power stream is deflected
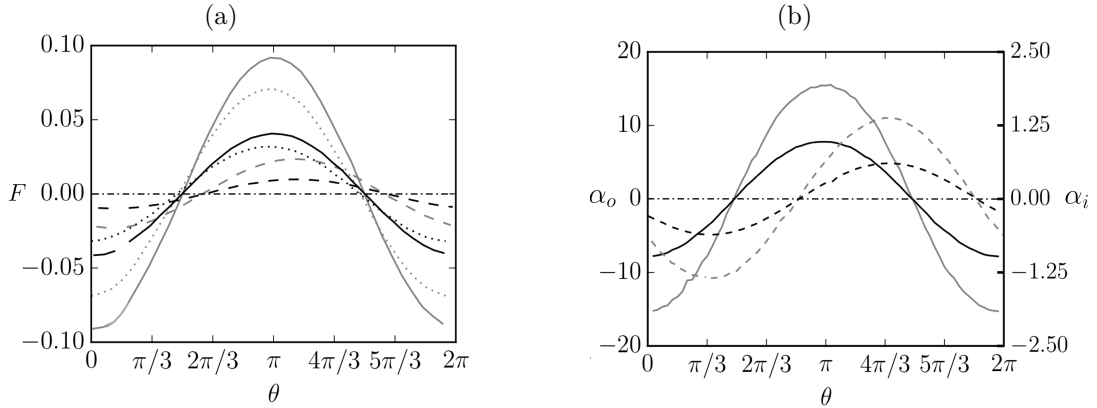
7

Fig. 5: FO properties along a full oscillation cycle at $Re = 88$ for F2D (gray) and F3D (black) simulations. Signals have been phase-averaged. (a) Inertia (F_i, dashed), pressure (F_p, dotted) and total (F, solid) vertical forces exerted by the two FCs through their respective outlet ports unto the power stream. (b) Power stream (α_i, dashed) and output jet (α_o, solid) deflection angles at the inlet of the MC and the NT, respectively.

to one side of the MC, it impinges on the convergent section of the cavity wall either above or below of the NT. At the stagnation point, the stream splits in two. The largest portion is driven through the NT into the QA, while a smaller part is driven along the nearest FC and reinjected at MC inlet thus providing advective momentum flux that acts on the power stream. At the same time, the pressure surge at the stagnation point pressurises the neighbouring FC thus effecting a pressure difference between opposing FCs. This pressure gradient from one FC outlet to that opposing it, and thus orthogonal to the power stream, results in a net momentum flux that also contributes in correcting the flow deflection. Needless to say, both F_p and F_i are balanced for the straight-jet solution, while the force equilibrium is unstable for the oscillating jet solution.

The total vertical force acting on the power stream can be thus split into its two main components as

$$F = F_i + F_p = \hat{\mathbf{y}} \cdot \left[\iint_S \mathbf{u}(\mathbf{u} \cdot \hat{\mathbf{n}}) \, dS + \iint_S p\hat{\mathbf{n}} \, dS \right]$$

where S covers both the lower and upper FC outlet planes and $\hat{\mathbf{n}}$ is the unit normal away from the FC exits.

Fig. 5(a) depicts the inertia (F_i, dashed), pressure (F_p, dotted) and total (F, continuous) vertical forces exerted by the combined effect of both FCs on the power stream along a full oscillation cycle, phased-averaged over several cycles. Shown are the forces for F2D (gray) and F3D (black) simulations at $Re = 88$. The correcting momentum flux exerted by the FCs is clearly dominated by pressure (dotted) rather than advection (dashed) for both the F2D (gray) and F3D (black) cases. The total momentum reinjection is also larger, by a factor of around 2, for F2D than F3D on account of the milder oscillation of the latter. The relative contribution of pressure and advection momentums to total force is not significantly modified from F2D to F3D, which seems to indicate that both grow fairly proportional to power stream deflection. The space-time symmetry of the solution is clear from all force signals and the maximum total momentum flux coincides with (and opposes) maximum power-stream deflection. There is however a clear phase lag between advective and pressure momentum fluxes, the former preceding the latter by about $\Delta\theta^{\text{F2D}} \simeq 25°$ and $\Delta\theta^{\text{F3D}} \simeq 27°$ of a full cycle for the F2D and F3D, respectively.

The evolution along one full oscillation cycle of the power stream deflection angle at MC inlet (α_i, dashed) and the output jet sweep angle at NT (α_o, solid) is shown in Fig. 5(b). These angles have been measured from flow velocity probes located on the symmetry plane at the IC exit and the NT, and averaged over the span for the three-dimensional run. The oscillation amplitude for F2D is about double that of F3D and much larger, by about a factor of 12, on the respective output jets than for the incoming power streams. There is also a phase lag from power stream to output jet deflection angles of around $295°$ ($296.1° \pm 5.9°$ and $294.5° \pm 3.4°$ for F2D and F3D, respectively). The output jet attains its maximum deflection around $5/6^{\text{th}}$ of a cycle after the power stream was at its maximum deflection.
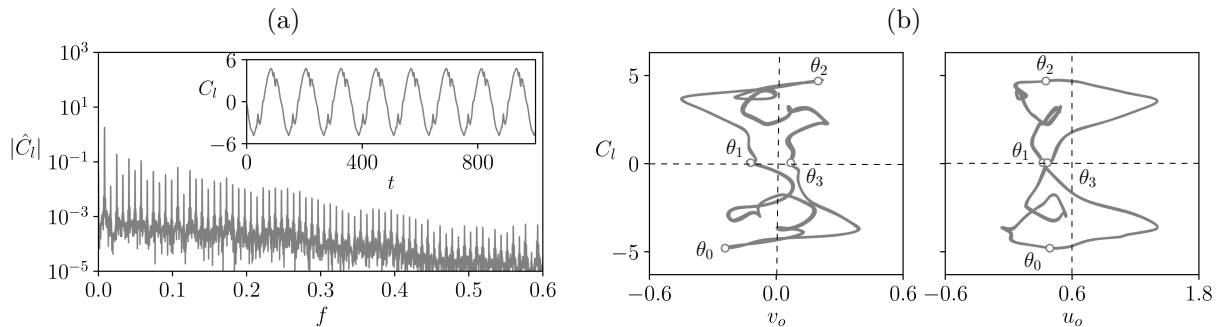
8

Fig. 6: Space-time-symmetry-broken periodic periodic state at $Re = 300$ for F2D case. (a) Spectrum $|\hat{C}_l|$ of the C_l time-series (shown in the inset). (b) Phase map projection on the (u_O, C_l) and (v_O, C_l) planes. Four equispaced instantaneous phases along a full oscillation cycle, as obtained from the C_l signal via Hilbert transform, are indicated with white circles and labelled θ_i, $i \in 0, 1, 2, 3$.
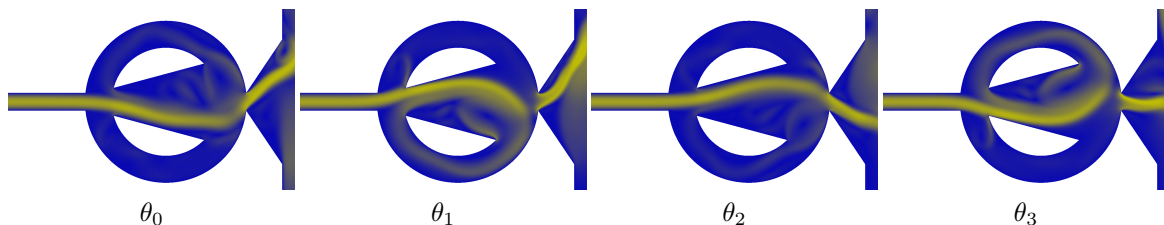

Fig. 7: Velocity field colourmaps of the periodic F2D-solution at $Re = 300$ at instants indicated with white circles in Fig. 6(b) and corresponding to equispaced phases $\theta_0, \theta_1, \theta_2$ and θ_3. Colour coding as for Fig. 2.

F2D solutions retain the space-time symmetry just described, with a slight degree of superposed chaotic fluctuations due to the jet instability, all the way up to $Re \simeq 290$. Beyond this point, the symmetry is finally disrupted, as exemplified by the (u_O, C_l) and (v_O, C_l) phase-map projections of Fig. 6(b) at $Re = 300$. The cycle remains qualitatively symmetric and the repetition of the main features of the trajectory are clearly identifiable after half a period, but the reflection operation does no longer produce a quantitative match. The solution remains mainly periodic, as the phase map trajectories wind around indefinitely following the same cycle, but the repetition is not exact and the phase map projections appear as a band rather than a thin line due to the mild chaotic fluctuations of the ouput jet. This is also clear from the C_l spectrum in Fig. 6(a), which shows a clear peak at frequency $f = 0.0082$ (corresponding to a time period $T = 121.95$) and harmonics, protruding from featureless broad-band noise. The frequency is lower at $Re = 300$ than it was at $Re = 88$, which points at a decrease of oscillation frequency as Reynolds number is increased. This behaviour belies that observed for fully turbulent FOs, which feature an increasing oscillation frequency. As a matter of fact, FOs may produce oscillating jets in the laminar regime, but this oscillation is later lost in the transitional regime and recovered again once the flow has become fully turbulent.

The velocity fields of Fig. 7, evenly distributed along a full oscillation cycle, provide further insight into the symmetry disruption of the periodic F2D solution. The attachment of the power stream to the straight wall of the IEs is remarkably more pronounced at $Re = 300$ than at $Re = 88$. While the internal flow is fully attached to IE$_l$ at θ_0, the sweeping jet leaves the FO with a large upward deflection angle. The output jet still points up, even more so, as the power stream has flipped and has started attaching to the IE$_u$ straight wall at θ_1. Advective momentum transfer along the FC$_l$ can be detected at this point with the naked eye, which was not the case at the lower $Re = 88$. The massflow going through the FC$_l$ joins the main power stream coming from the IC and helps fulfil the complete attachment onto IE$_u$ at θ_2. Once this is accomplished, the advective momentum transport across the FCs is no longer detectable and the output jet has reached its lowest angle. At θ_3 the power stream has flipped again, feedback advective momentum can be spotted on the FC$_u$ and the jet leaves almost horizontally. Comparing the snapshots at phases taken half
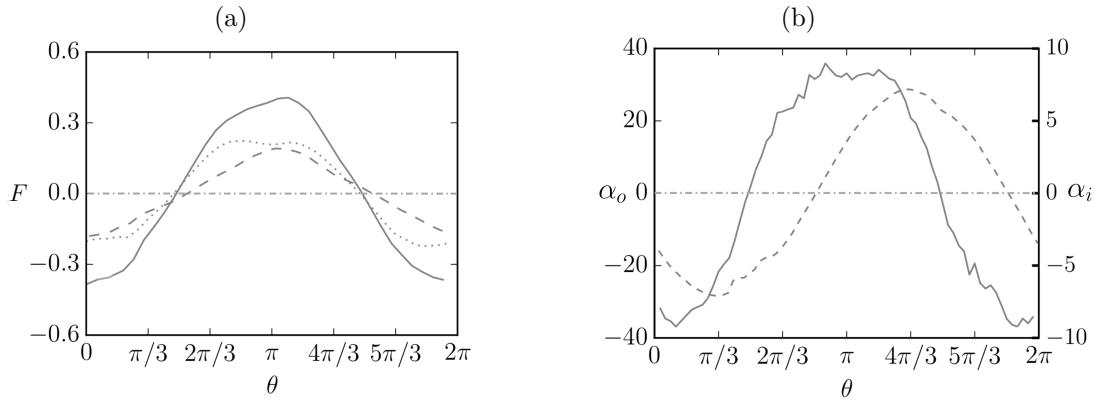
9

Fig. 8: FO properties along a full oscillation cycle at $Re = 300$ for F2D simulations. Signals have been phase-averaged. (a) Inertia (F_i, dashed), pressure (F_p, dotted) and total (F, solid) vertical forces exerted by the two FCs through their respective outlet ports unto the power stream. (b) Power stream (α_i, dashed) and output jet (α_o, solid) deflection angles at the inlet of the MC and the NT, respectively.

a cycle apart (θ_0 vs θ_2 and θ_1 vs θ_3), the space-time symmetry inside the FO cavity is still remarkable, but the output jet has a clear upward bias. A solution that is symmetry-conjugate to the one shown in Fig. 7 does of course exist and either one of the two might be obtained depending on the initial conditions.

The contribution of pressure (F_p, dashed) and advective (F_i, dotted) to total (F, solid) momentum injection at FCs exit is comparable at $Re = 300$, as shown in Fig. 8(a). The vertical correction forces exerted on the power stream are larger than those occurring at $Re = 88$ and pressure has lost its predominance over advection. The latter does no longer feature a clear peak and a kind of plateau exceeding a quarter cycle has replaced it. Pressure force still lags behind advective momentum, but barely so. The deflection angle at the inlet of the MC (α_i) follows a pattern very similar to that observed for $Re = 88$, albeit with a somewhat larger amplitude as shown in Fig. 8(b). The output jet angle, as measured at the NT, however, has a clear upward bias. The maximum upward angle has a similar value to the maximum downward deflection, but is sustained for a longer time during which the jet remains pretty much attached to the upper wall of the ND through the Coandă effect. As was the case at the lower Reynolds number, the power stream leads the output jet deflection by about $5/6^{\text{th}}$ of the full cycle.

4. Stability of two-dimensional solutions to spanwise-dependent perturbations

Systems featuring homogeneous boundary conditions along an extended spatial direction can often be treated as two-dimensional at sufficiently low values of the Reynolds number. Away from the bounds of the domain in the extended direction, the flow is steady and practically two-dimensional. Three-dimensional perturbations may however be amplified beyond a certain critical Re and lead to fully three-dimensional solutions.

We have performed a linear stability analysis of the steady solution to spanwise-periodic perturbations of varying wavelength in order to determine the critical Reynolds number and wavenumber. Fig. 9 depicts the eigenvalue with the largest real part, which happens to be real, as a function of wavenumber κ_z for three different Reynolds numbers. The first wavenumber to bifurcate is $\kappa_{z_3} = 0.483$, roughly corresponding to a wavelength $\lambda_{z_3} = 2\pi/\kappa_{z_3} = 13$, at $Re_3 \simeq 67$. This wavelength is sufficiently large that actual FO devices, which are narrow in the spanwise direction, can hardly accomodate it. Actual three-dimensionality will therefore be driven by the bounding walls at these low values of the Reynolds number.

In some cases, three-dimensionality is preceded by the onset of time-dynamics, such that Floquet stability analysis is required to gauge the instability modes and their growth rates. Such is the case of the flow past a cylinder of circular [26, 27] or square [28] cross-section, for which a von Kármán vortex street is already in place by the time three-dimensionality kicks in. For the simple FO under scrutiny here, the bifurcation
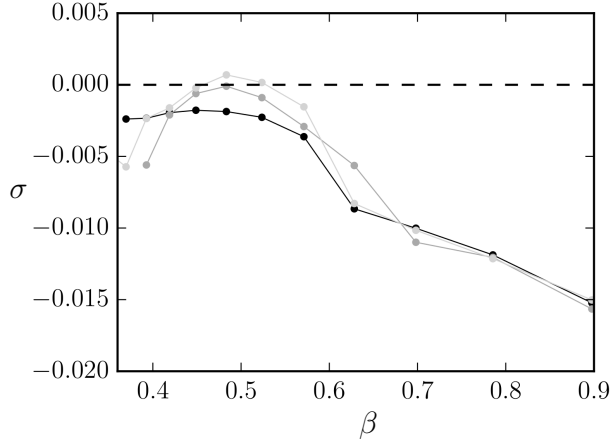
10

Fig. 9: Eigenvalue σ with the largest real part as a function of Re and wavenumber κ_z. Shown are $Re = 66$ (black), $Re = 67$ (dark gray) and $Re = 68$ (light gray). Bullets indicate actually tested wavenumbers.

that breaks the spanwise-invariance anticipates the Hopf bifurcation that triggers time-dependence. It may nevertheless be still useful to try and forecast the spanwise periodicity of fully three-dimensional solutions at any given value of the Reynolds number by determining the fastest growing modes for the underlying time-dependent two-dimensional solution. Although the wavelength of the linear instability needs not coincide with the spanwise size of actual three-dimensional flow structures away from the bifurcation point, it can still guide the choice of the domain's minimum spanwise extent required for reliable and accurate three-dimensional computations.

Out-of-the-box Floquet analysis does not apply here because the two-dimensional solution is not perfectly time-periodic, on account of the mild chaotic fluctuations introduced in the temporal dynamics by the output jet instability. To overcome this obstacle, we have devised a method that relies solely on time-stepping to compute the most unstable *pseudo*-Floquet multiplier of the two-dimensional oscillating-jet solution. The method consists of two steps. First, the two-dimensional, almost-periodic, time-dependent solution, $\mathbf{U} = \mathbf{U}(x, y; t) = (U, V)$, is fully resolved in the two-dimensional domain by time-integrating past all initial transients. Then, a tiny three-dimensional random perturbation of order $\epsilon \ll 1$, $\tilde{\mathbf{u}}_0 e^{i\kappa_z z} + \text{cc}$, with $\tilde{\mathbf{u}}_0 = \tilde{\mathbf{u}}(x, y; 0) = (\tilde{u}, \tilde{v}, \tilde{w})_0$ and cc denoting complex conjugation, is added and the flow evolved further within the simplest three-dimensional domain by considering a single Fourier mode of wavenumber κ_z. An additive decomposition is applied to the instantaneous perturbed velocity field following

$$\mathbf{u}(x, y, z; t) = \mathbf{U}(x, y; t) + \tilde{\mathbf{u}}(x, y; t)e^{i\kappa_z z} + \text{cc}. \tag{2}$$

Plugging the expression above back into the Navier-Stokes equations, i.e. Eq. 1, we find the equations for the perturbation field as

$$\frac{\partial \tilde{\mathbf{u}}}{\partial t} + \underbrace{(\tilde{\mathbf{u}} \cdot \nabla)\tilde{\mathbf{u}}}_{\mathcal{O}(\epsilon^2)} + (\mathbf{U} \cdot \nabla)\tilde{\mathbf{u}} + (\tilde{\mathbf{u}} \cdot \nabla)\mathbf{U} = -\nabla\tilde{p} + \frac{1}{Re}\nabla^2\tilde{\mathbf{u}}$$

$$\nabla \cdot \tilde{\mathbf{u}} = 0 \tag{3}$$

where $\tilde{p}$ is the perturbation pressure field and the nonlinear term has negligible effects on the dynamics as long as the perturbation velocity field remains of order ϵ. There is no need to implement the linearised Navier-Stokes equations of (3). The full non-linear equations in (1) can be evolved in time and the first and only Fourier mode tracked as long as it remains within the linear regime. After some initial transients, the perturbation field will naturally align with the fastest growing mode (or the slowest decaying) and thus provide information on the stability of the underlying two-dimensional flow. The analysis is analogous to that followed by Sarwar and Mellibovsky [29] in analysing the spanwise stability of two-dimensional chaotic
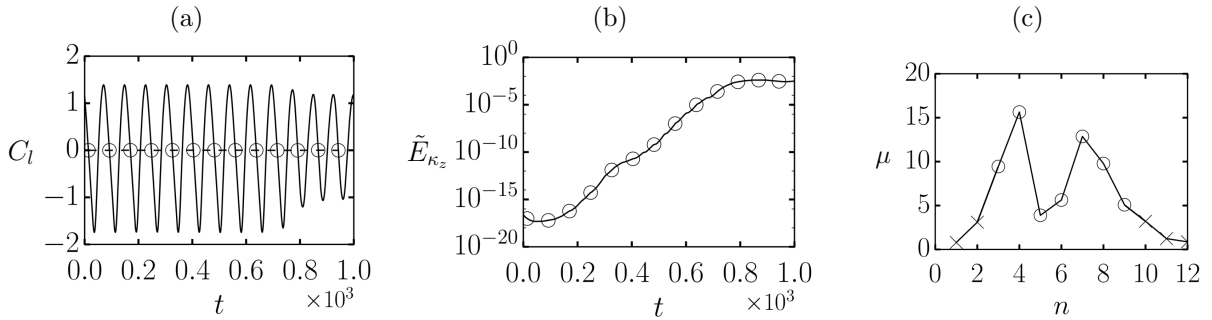
11

Fig. 10: Estimation of Floquet multiplier from time traces of C_l and kinetic energy $\tilde{E}_{\kappa_z}$ of the perturbation velocity field at $Re = 100$; (a) C_l time series with Poincaré section defined at phase $\phi = \pi/2$ (crossings marked with circles). (b) Linear growth of the perturbation velocity kinetic energy $\tilde{E}_{\kappa_z}$ for $\kappa_z = \frac{2\pi}{13}$. (c) Cycle-average Floquet multiplier $\mu(n)$ as a function of cycle number n. Circles indicate μ values within the linear regime, while crosses denote either initial transients or nonlinear saturation and are not valid for computing statistics.

vortex-shedding past a circular cylinder at $Re = 2000$. A Poincaré section is defined, here based on the instantaneous phase of the C_l signal, and the mean Floquet multiplier over the corresponding cycle estimated as

$$\mu = \sqrt{\frac{\tilde{E}_{\kappa_z}^n}{\tilde{E}_{\kappa_z}^{n-1}}}, \tag{4}$$

where $\tilde{E}_{\kappa_z}^n$ is the kinetic energy contained in the perturbation velocity field $\tilde{\mathbf{u}}(x, y; t^n)\mathbf{e}^{\mathbf{i}\kappa_z z}$ at the time t^n of Poincaré crossing n.

Fig. 10 exemplifies the procedure at $Re = 100$. The C_l signal used in defining the Poincaré section is shown in Fig. 10(a), and all Poincaré crossings are marked with circles. The evolution of the kinetic energy $\tilde{E}_{\kappa_z}$ contained in the perturbation velocity field is shown in Fig. 10(b). After a short initial transient, the energy grows steadily closely following the exponential trend that is typical of the linear regime of perfectly periodic solutions, before finally saturating at nonlinear levels. Saturation corresponds to nonlinear interaction of the perturbation velocity fields that feeds energy back onto the two-dimensional flow, the effect of which can be clearly observed towards the end of the C_l signal in Fig. 10(a) as a clear disruption of the original oscillation amplitude. The energy at the Poincaré crossings, marked with circles in Fig. 10(b), has been used to estimate the average Floquet multiplier over each FO cycle and the sequence plotted in Fig. 10(c). The imperfect exponential growth is to be ascribed to the presence of chaotic fluctuations that modulate the two-dimensional underlying flow stability from cycle to cycle. The pseudo-Floquet multiplier fluctuates over time and can therefore only be defined statistically. A sharp value is not to be expected as outcome, as chaotic fluctuations instantaneously affect the stability of the two-dimensional solution in a way that growth (or decay) is not purely modal.

Once in the linear growth regime, the perturbation field must be understood as the least stable pseudo-eigenmode. It is not a mode proper, as the two-dimensional underlying flow is neither steady nor periodic and the instability is not perfectly modal, but it still contains valuable information as to where the instability is actually located. Fig. 11(a) depicts the two-dimensional spanwise vorticity field Ω of the underlying solution at one of the Poincaré crossings within the linear regime, alongside the corresponding perturbation cross-stream vorticity field $\tilde{\omega}_y$ (panel b) at the same instant. The three-dimensional instability is clearly growing fastest in the proximal jet region, particularly so along the curved braids that trail from the last issued vortex core. Growing three-dimensionality is conspicuously absent within the FO cavity and in the distal jet region, which points at a local spanwise instability of the high shear regions of the outcoming jet. Three-dimensionalisation of the flow inside the FO can therefore be attributed to the result of an external jet instability, whose effect, as we will shortly see, is that of retarding the onset of time-dynamics.

The determination of the fastest growing three-dimensional perturbation has been extended to varying wavenumber κ_z and $Re \in \{100, 200, 300\}$ in Fig. 12. The error bars convey variability in the growth rate

12

Fig. 11: Least stable pseudo-eigenmode at $Re = 100$. (a) Spanwise vorticity $\Omega_z \in [-5, 5]$ colourmap of the two-dimensional flow. (b) Cross-flow vorticity $\tilde{\omega}_y$ (symmetric arbitrary range) at the same instant, well within the linear growth regime.
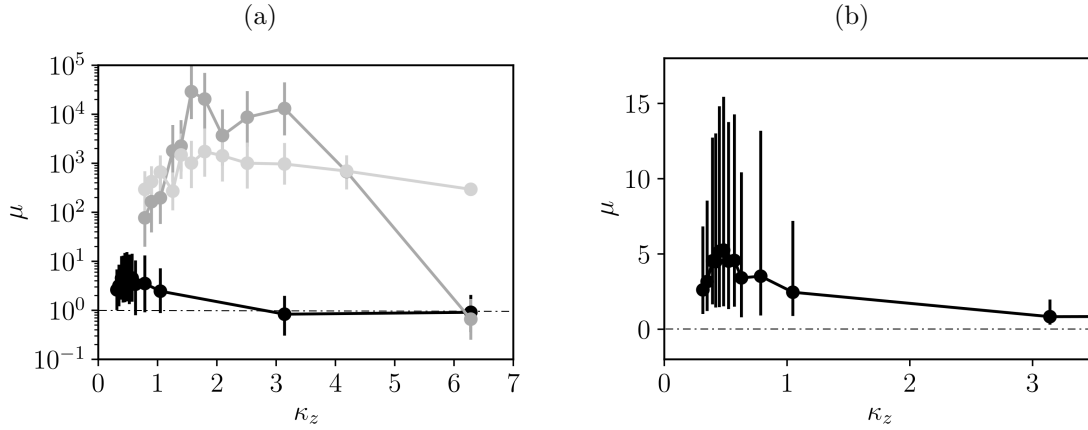

Fig. 12: (a) Most unstable pseudo-Floquet multiplier μ vs wavenumber $\kappa_z = \frac{2\pi}{L_z}$ at $Re = 100$ (black), $Re = 200$ (dark gray) and $Re = 300$ (light gray). (b) A detail of the $Re = 100$ case. Error bars indicate indicate the standard deviation along the linear-growth regime and across multiple determinations starting from different initial conditions.
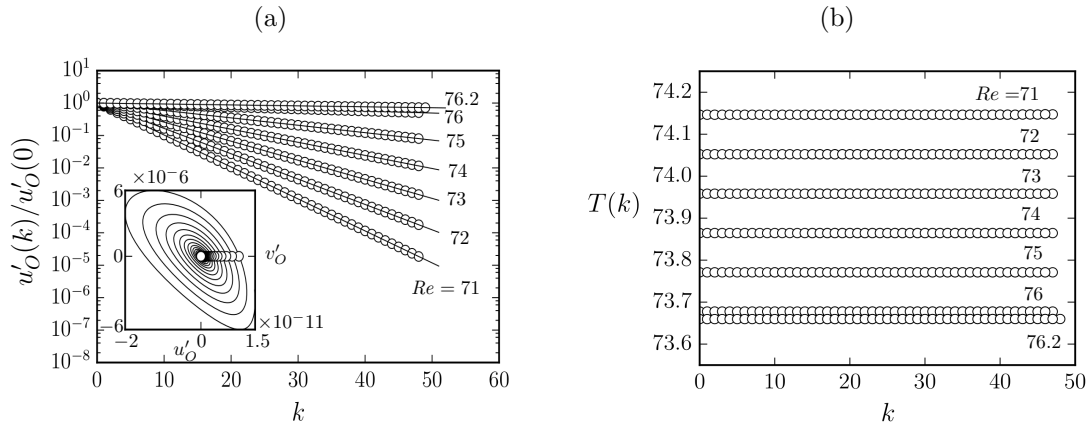
13

Fig. 13: (a) Exponential decay of the perturbation field u'_O along the sequence of crossings of the Poincaré section diefined by $\mathcal{S} = \{(\mathbf{u}', p') : v'_O = 0, \dot{v}'_O > 0\}$. Each set of bullets corresponds to sequential Poincaré crossings for T2D simulation at a different $Re \in [71, 76.2]$. Solid lines indicate least-squares exponential fits. The inset shows a continuous-time phase map projection on the (u'_O, v'_O) plane. (b) Flight time $T(k) = t^k - t^{k-1}$ between consecutive Poincaré crossings.

that might be expected at different instants along the mildly chaotic two-dimensional oscillating-jet solution. At $Re = 100$, the spanwise wavenumber of the instability may already range from very long to very short, the most unstable corresponding to $\kappa_z = 0.483$. Two separate instability modes seem to compete instead at $Re = 200$, the most unstable having $\kappa_z \simeq 1.57$, followed by a second mode, somewhat shorter with $\kappa_z \simeq 3$. The former mode seems to remain dominant at $Re = 300$, albeit slightly shifted to $\kappa_z \simeq 1.8$, while the second mode appears to have vanished. The large error bars at $Re = 200$ and 300 are a result of the extremely fast modal growth, which leaves the linear regime in so few Poincaré crossings, that statistics become unreliable.

The long wavelength of the fastest growing perturbations, in combination with their location in the external flow region, suggests that the two-dimensional analysis of the FO might still be valuable for narrow practical implementations despite the obvious effects of bounding walls.

5. The onset of time-dynamics

As we have already seen, the output jet of the FO starts oscillating somewhere in the range $Re \in [75, 88]$ regardless of whether the two-dimensional, full (F2D) or truncated (T2D) at nozzle exit, or three-dimensional (F3D) domain is considered. Here we follow the time-stepping-based approach of An et al. [30] in order to investigate the Hopf bifurcation that is responsible for the onset of time-periodicity in F2D simulations. Namely, we investigate the evolution of small perturbations on top of the stable symmetric-jet steady-state solution as the onset of time dynamics is approached by increasing the Reynolds number. While stable, whenever the steady state is perturbed, the perturbation velocity field decays and the symmetric-jet solution is asymptotically recovered. The fashion and rate with which the perturbation vanishes provide insight into the type and proximity, respectively, of the bifurcation under scrutiny.

In the case of a Hopf bifurcation, which anticipates the onset of time-dynamics, all field variables approach exponentially the steady state following a damped oscillatory pattern. To illustrate this, we define the perturbation velocity at the centre of the FO cavity as $\mathbf{u}'_O = (u'_O, v'_O) \equiv \mathbf{u}(0, 0; t) - \mathbf{u}_{SJ}(0, 0)$, where $\mathbf{u}$ and $\mathbf{u}_{SJ}$ are the instantaneous and symmetric-jet steady-state velocity fields, respectively. The perturbation velocity in the centre of the cavity asymptotically spirals towards anihilation, as shown in the inset of Fig. 13(a) for $Re = 71$. The steady state is a stable focus, meaning that the leading eigenmode is a complex-conjugate pair. The real and imaginary parts of the leading eigenvalue can be estimated by using a purposely devised Poincaré section $\mathcal{S} = \{(\mathbf{u}', p') : v'_O = 0, \dot{v}'_O > 0\}$ and then recording the sequence of $u'_O(k)$ and flight times $T(k) = t^k - t^{k-1}$ at successive Poincaré crossings. In the linear regime, once the initial transients have
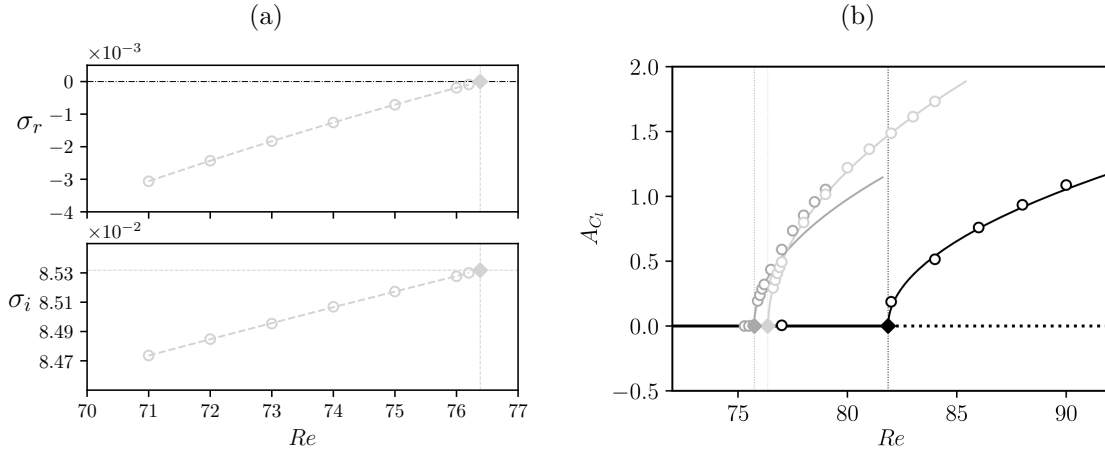
14

Fig. 14: Hopf bifurcation in the FO. (a) Real (σ_r, top) and imaginary (σ_i, bottom) parts of the leading eigenvalue for T2D as the bifurcation point is approached by increasing Re. A quadratic fit (dashed line) estimates the Hopf bifurcation at $Re_{\mathrm{H}_{2t}} = 76.4$ with angular frequency $\omega_{\mathrm{H}_{2t}} = \sigma_i(Re_{\mathrm{H}_{2t}}) = 0.0853$. (b) Lift coefficient amplitude A_{C_l} vs Re of the oscillating-jet periodic solution for the F2D (dark gray), T2D (light gray) and F3D (black) cases. Circles indicate actually computed nonlinear solutions while error bars denote variability due to chaotic fluctuations. Lines correspond to square-root fits of the points closest to the bifurcation. Diamonds indicate the bifurcation point as predicted by the fits. The vertical dotted lines indicate the Hopf bifurcations as estimated from perturbation decay analysis (see panel a).

been overcome and the perturbation has aligned with the least unstable eigenmode, the imaginary part of the leading eigenvalue may be estimated from

$$T = \lim_{k \to \infty} T(k) \qquad \longrightarrow \qquad \sigma_i = \frac{2\pi}{T}. \tag{5}$$

A least-squares exponential fit to the tail of the decaying set $u'_O(k)/u'_O(0)$, with $u'_O(0)$ taken already sufficiently deep into the linear regime, yields the multiplier μ, which can then be used to esimate the real part of the leading eignevalue as

$$\frac{u'_O(k)}{u'_O(0)} = \mu^k \qquad \longrightarrow \qquad \sigma_r = \frac{1}{T} \log \mu. \tag{6}$$

Fig. 13(a) shows the exponential decay of $u_O(k)$ along the sequence of Poincaré crossings k for a range of $Re \in [71, 76.2]$. The exponential fits are excellent and the decay rate is seen to decrease with Re, a clear indication that the bifurcation is being approached. Fig. 13(b) records the sequence of flight times between consecutive Poincaré crossings, which are very stable across the full linear-growth regime. The imaginary and real parts of the leading eigenvalue extracted from the fits in Fig. 13 and employing Eqs. (5)-(6) are plotted against Reynolds number in Fig. 14(a). A quadratic fit (dashed line) to the last few points before the zero-crossing of the real part σ_r of the leading eigenvalue places the Hopf bifurcation for the T2D case at $Re_{\mathrm{H}_{2t}} = 76.4$. Beyond this point perturbations are expected, and indeed seen, to grow and the flow departs from the steady symmetric-jet solution. A second quadratic fit to the last few points of the imaginary part σ_i provides a fair estimation of the angular frequency at the Hopf point, which yields $\omega_{\mathrm{H}_{2t}} = \sigma_i(Re_{\mathrm{H}_{2t}}) = 0.0853$, corresponding to a Strouhal frequency $St_{\mathrm{H}_{2t}} = \omega_{\mathrm{H}_{2t}}/(2\pi) = 0.0136$. This is compatible with the frequency $St(88) = 0.0132$ reported for the fully nonlinear solution at a slightly higher $Re = 88$ presented in §3 and the decreasing trend observed upon increase to $Re = 100$ and then further to $Re = 300$ when analysing convergence in §2.

In order to ellucidate the nature, subcritical or supercritical, of the Hopf bifurcation, a few non-linear oscillating-jet solutions have been computed beyond $Re_{\mathrm{H}_{2t}}$. The combined lift coefficient oscillation amplitude $A_{C_l} \equiv C_l^{\max} - C_l^{\min}$ has been plotted as a function of Re in Fig. 14(b) for the F3D (black), F2D (dark gray) and T2D (light gray) cases. Filled circles denote actually computed oscillating-jet solutions and

15

a square-root fit of the form

$$A_{C_l} = A_{C_l}^{\mathrm{bif}} + K\sqrt{Re - Re_{\mathrm{bif}}}, \tag{7}$$

with fitting parameters $A_{C_l}^{\mathrm{bif}}$, Re_{bif} and K, has been applied to the few leftmost points of each case to allow extrapolation of the bifurcation point. The offset term $A_{C_l}^{\mathrm{bif}}$ of the fit vanishes in all three cases, which indicates that the bifurcation point is a supercritical Hopf. As a matter of fact, $Re_{\mathrm{bif}}^{\mathrm{t2d}}$ coincides with $Re_{\mathrm{H}_{2t}}$ to within the expected accuracy of the methods employed.

It must be borne in mind that the oscillating-jet instability introduces mild chaotic fluctuations that perturb the periodicity of the bifurcated solutions. Accordingly, all solutions in Fig. 14(b) computed on the full domain are represented by a point that indicates the mean oscillation amplitude and an error bar that expresses the variability. In most cases the variability is imperceptible to the naked eye and only the F3D case that is closest to the bifurcation point features actually discernible fluctuations.

The only difference between F2D and T2D cases is the use or not of an external QA. T2D crops the domain at the exit of the ND and imposes on it the average pressure measured at this precise location in F2D simulations with the same Re with the sole aim of understanding the output jet effect on the FO cavity instability that triggers the oscillation. The first remarkable effect of eliminating the QA is that chaotic fluctuations are suppressed altogether, which points at an oscillating external jet instability as the culprit. The second consequence of truncating the domain is that the Hopf bifurcation is slightly retarded to $Re_{\mathrm{H}_2} = 76.4$ from 75.7. This suggests that chaotic fluctuations, although mild and originating outside of the domain, are capable of triggering the FO cavity instability a little earlier than it would naturally occur in a noiseless controlled environment.

When the spanwise direction is taken into consideration in F3D simulations, the Hopf bifurcation point remains supercritical but is pushed back to higher $Re_{\mathrm{H}_3} = 82.1$. The three-dimensionalisation of the flow at $Re_3 = 67$, introduces a spanwise modulation in the jet that permeates into the FO cavity. This slighlty wavy sheet into which the power stream turns appears to be more robust to the instability that triggers the oscillation, much in the way that a wavy plate has better endurance to buckling under compression along a direction normal to the plain containing the wavy pattern.

The nature -supercritical for all three cases- of the bifurcation, the similar oscillation frequency, and the resemblance of the resulting fully nonlinear oscillating solutions among all three cases considered, leads us to conclude that the mechanism that triggers the onset of time-dynamics is the same, and that it relies on an intrinsic instability of the FO cavity resulting from its internal geometry.

6. The loss of the space-time symmetry

The oscillating-jet solutions progressively develop into escalating nonlinearity as the Reynolds number is increased. Chaotic fluctuations also build up, but the space-time symmetry inherited from the steady base flow remains distinctly identifiable in both phase-maps and flow snapshots taken half a period apart. At $Re = 300$, however, the symmetry has been finally lost for F2D simulations and the output jet has a bias to spend more time to one side of the QA than the other. This is suggestive that a pitchfork bifurcation of cycles has taken place.

In order to characterise the symmetry loss, a symmetry parameter must be defined. To do so, a pair of Poincaré sections have been set up at $C_l = 0$, one with the additional condition that $\dot{C}_l > 0$, the other with $\dot{C}_l < 0$. Phase map trajectories pierce one and the other of the Poincaré sections in an alternate fashion, such that the evolution between two consecutive crossings $k-1$ and k becomes a representation of a half cycle. The space-time symmetry of a (pseudo-)periodic solution demands that the combined drag coefficient C_d on IE$_u$ and IE$_l$ repeats every half cycle, so that a symmetry parameter defined as

$$\psi \equiv |C_d(t_k) - C_d(t_{k-1})|$$

must exactly vanish for space-time-symmetric solutions and depart from zero for symmetry-broken solutions. In the absence of chaotic fluctuations, ψ is expected to converge onto a constant value. Otherwise, ψ is randomly distributed and a mean and standard deviation can be extracted from the statistically converged
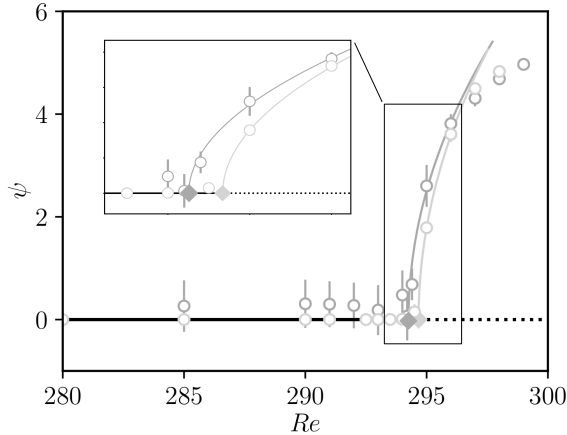
16

Fig. 15: Pitchfork bifurcation diagram for T2D (light gray) and F2D (dark gray) pseudo-periodic solutions. Circles denote mean value and errorbars plus/minus two standard deviations of the symmetry parameter ψ, expressed as a function of Re. Full lines denote square-root fits to the data and filled diamonds indicate the predicted pitchfork points.

$\psi(k)$ sequence. This is shown for both T2D (light gray) and F2D (dark gray) simulations in Fig. 15, where the circles denote the mean, and the errorbars plus-minus two standard deviations (95% confidence interval). The symmetry parameter remains negligible for T2D all the way up to $Re < Re_{P_{2t}} \simeq 294.6$. From this point on, the increasing trend is well adjusted by a square-root fit analogue to that in (7) to the few points closest to the bifurcation. The vanishing additive parameter indicates that the pitchfork is supercritical. For F2D, despite its probabilistic nature due to chaotic fluctuations, the statistical average of ψ is indistinguishable from zero up to $Re < Re_{P_2} \simeq 294.2$ with over 99% confidence. Beyond the bifurcation point, ψ clearly departs from symmetry and a square-root fit to the statistical average of the first few points confirms supercriticality. The situation is far more complex when considering the full three-dimensional domain and will not be explored here.

7. Conclusions

We have characterised the various flow states and analysed the onset of time dynamics for a spanwise-extended laminar fluidic oscillator operating at very low values of the Reynolds number. The flow remains two-dimensional, steady and reflection-symmetric all the way up to $Re_3 \simeq 67$, beyond which point the span-wise invariance is broken and the flow becomes three-dimensional. The resulting nonlinear three-dimensional solutions remain steady. The critical wavenumber is $\kappa_{z_3} = 0.483$, which corresponds to a spanwise wave-length $\lambda_{z_3} = 13$, as a thorough analysis of the fastest growing three-dimensional perturbations shows. Practical realisations of fluidic oscillators are usually much narrower than the first destabilised spanwise mode, so that three-dimensionallity in this regime would generally be driven by side-wall effects. However, the infinite-spanwise-domain approach becomes gradually more valid, as the most unstable spanwise modes of the underlying two-dimensional solution shift to shorter wavelenghts with increasing Re.

It is only by increasing the Reynolds number further that the output jet starts oscillating, following a supercritical Hopf bifurcation at $Re_{H_3} = 82.1$. The oscillation is mainly driven by pressure momentum that the feedback channels capture at mixing chamber exit and reinject transversally at mixing channel inlet, just downstream from the inlet channel. Nonetheless, the Coandă effect fails to completely attach the power stream to the straight walls of the internal elements and the output jet sweep angle is only moderate. Full attachment is instead fulfilled if the spanwise waviness is duely suppressed by considering a two-dimensional domain. In this case the jet oscillates with much larger amplitude and the onset of time-periodicity is considerably advanced to $Re_{H_2} = 75.7$. Spanwise waviness can therefore be considered a stabilising factor.

17

Both for the two- and the three-dimensional FOs, time-periodicity arises together with mild chaotic fluctuations, which is not a usual feature of Hopf bifurcations. As a matter of fact, some mediating bifurcations must be at play that we have not been able to identify. Perhaps a very mild and imperceptible subcriticality or a classic Ruelle-Takens transition scenario. The two-dimensional domain has been truncated at the nozzle exit and the boundary conditions adapted from full domain simulations to cast light on the origin of the chaotic fluctuations. The fact that chaos is completely suppressed on the truncated domain indicates that its origin must be traced to an external oscillating jet instability. Besides, the Hopf bifurcation remains supercritical and is only slightly pushed forward to $Re_{\mathrm{H_2}} = 76.4$. This confirms that the triggering mechanism for the oscillation is an intrinsic instability of the FO cavity geometry and that the only effect of the mild external fluctuations is to slighlty advance the onset of the instability.

In spite of the mild chaotic fluctuations, the original reflectional symmetry of the steady state is broadly retained as a space-time symmetry (the flow is invariant under evolution over half a period followed by reflection about the mid plane) for a wide range of Re. For the two-dimensional FO, this symmetry is finally disrupted in a supercritical pitchfork bifurcation of cycles at $Re_{\mathrm{P_2}} = 294$. From this point on, the jet acquires a bias in its oscillation to one side. Two mutually symmetric solutions exist, and which is actually reached depends on the initial conditions.

The effects of spanwise bounding walls on actual implementations of the laminar FO under scrutiny here remains to be analysed. Narrow configurations at low Reynolds numbers that undergo very long spanwise-invariance-breaking instabilities may behave very differently from the extended FO investigated here.

Acknowledgements

References

[1] S. Raghu. Fluidic oscillators for flow control. *Expt. Fluids*, 54(2):1455, 2013.

[2] J. Gregory and M. N. Tomac. A review of fluidic oscillator development and application for flow control. In *43rd AIAA Fluid Dynamics Conference*, page 2474, 2013.

[3] D. M. Facteau, T. A. Cobb, and M. D. Hyman. Fluidic oscillator, November 24 1992. US Patent 5,165,438.

[4] S. Raghu. Feedback-free fluidic oscillator and method, July 3 2001. US Patent 6,253,782.

[5] F. Ostermann, R. Woszidlo, C. N. Nayeri, and C. O. Paschereit. Phase-averaging methods for the natural flowfield of a fluidic oscillator. *Amer. Inst. Aeronau. & Astro. J.*, 53(8):2359–2368, 2015.

[6] R. Woszidlo, H. Nawroth, S. Raghu, and I. Wygnanski. Parametric study of sweeping jet actuators for separation control. In *5th Flow Control Conference*, page 4247, 2010.

[7] R. Woszidlo and I. Wygnanski. Parameters governing separation control with sweeping jet actuators. In *29th AIAA Applied Aerodynamics Conference*, page 3172, 2011.

[8] M. Metka and J. W. Gregory. Drag reduction on the 25-deg ahmed model using fluidic oscillators. *ASME J. Fluid Engng*, 137(5), 2015.

[9] D. Guyot, B. Bobusch, C. O. Paschereit, and S. Raghu. Active combustion control using a fluidic oscillator for asymmetric fuel flow modulation. In *44th AIAA/ASME/SAE/ASEE Joint Propulsion Conference & Exhibit*, page 4956, 2008.

[10] L. Agricola, R. Prenter, R. Lundgreen, M. Hossain, A. Ameri, J. Gregory, and J. Bons. Impinging sweeping jet heat transfer. In *53rd AIAA/SAE/ASEE Joint Propulsion Conference*, page 4974, 2017.

[11] C. Camci and F. Herr. Forced convection heat transfer enhancement using a self-oscillating impinging planar jet. *J. Heat Trans.*, 124(4):770–782, 2002.

[12] M. A. Hossain, L. Agricola, A. Ameri, J. W. Gregory, and J. P. Bons. Effects of curvature on the performance of sweeping jet impingement heat transfer. In *2018 AIAA Aerospace Sciences Meeting*, page 0243, 2018.

[13] M. A. Hossain, R. Prenter, R. K. Lundgreen, A. Ameri, J. W. Gregory, and J. P. Bons. Experimental and numerical investigation of sweeping jet film cooling. *J. Turbomach.*, 140(3), 2018.

[14] Y. Wu, S. Yu, and L. Zuo. Large eddy simulation analysis of the heat transfer enhancement using self-oscillating fluidic oscillators. *Int. J. Heat Mass Transfer*, 131:463–471, 2019. ISSN 0017-9310.

[15] G. Raman, S. Packiarajan, G. Papadopoulos, C. Weissman, and S. Raghu. Jet thrust vectoring using a miniature fluidic oscillator. *Astrophys. J.*, 109(1093):129–138, 2005.

[16] J. W. Gregory, J. P. Sullivan, and S. Raghu. Visualization of jet mixing in a fluidic oscillator. *J. Visual.*, 8(2):169–176, 2005.

18

[17] J. W. Gregory, J. P. Sullivan, G. Raman, and S. Raghu. Characterization of the microfluidic oscillator. *Amer. Inst. Aeronau. & Astro. J.*, 45(3):568–576, 2007.

[18] M. N. Tomac and J. Gregory. Frequency studies and scaling effects of jet interaction in a feedback-free fluidic oscillator. In *50th AIAA Aerospace Sciences Meeting including the New Horizons Forum and Aerospace Exposition*, page 1248, 2012.

[19] M. N. Tomac and J. W. Gregory. Internal jet interactions in a fluidic oscillator at low flow rate. *Expt. Fluids*, 55(5):1730, 2014.

[20] C. E. Spyropoulos. A sonic oscillator. In *Proceedings of the Fluid Amplification Symposium*, volume Vol. III, pages 27–52, 1964.

[21] W. Gaylord and V. Carter. Fluerics. 27. Flueric temperature-sensing oscillator design. Technical report, Harry Diamond Labs Washington DC, 1969.

[22] B. C. Bobusch, R. Woszidlo, J. M. Bergada, C. N. Nayeri, and C. O. Paschereit. Experimental study of the internal flow structures inside a fluidic oscillator. *Expt. Fluids*, 54(6):1559, 2013.

[23] R. Woszidlo, F. Ostermann, C. N. Nayeri, and C. O. Paschereit. The time-resolved natural flow field of a fluidic oscillator. *Expt. Fluids*, 56(6):125, 2015.

[24] M. Baghaei and J. M. Bergada. Analysis of the forces driving the oscillations in 3d fluidic oscillators. *Energies*, 12(24): 4720, 2019.

[25] C.D. Cantwell, D. Moxey, A. Comerford, A. Bolis, G. Rocco, G. Mengaldo, D. De Grazia, S. Yakovlev, J.-E. Lombard, D. Ekelschot, B. Jordi, H. Xu, Y. Mohamied, C. Eskilsson, B. Nelson, P. Vos, C. Biotto, R.M. Kirby, and S.J. Sherwin. Nektar++: An open-source spectral/hp element framework. *Comp. Phys. Commu.*, 192:205 – 219, 2015.

[26] R. D. Henderson and D. Barkley. Secondary instability in the wake of a circular cylinder. *Phys. Fluids*, 8(6):1683–1685, 1996.

[27] B. R. Noack and H. Eckelmann. A global stability analysis of the steady and periodic cylinder wake. *J. Fluid Mech.*, 270: 297–330, 1994.

[28] H. M. Blackburn and J. M. Lopez. On three-dimensional quasiperiodic floquet instabilities of two-dimensional bluff body wakes. *Phys. Fluids*, 15(8):L57–L60, 2003.

[29] W. Sarwar and F. Mellibovsky. Characterization of three-dimensional vortical structures in the wake past a circular cylinder in the transitional regime. *Phys. Fluids*, 32(7):074104, 2020. doi: 10.1063/5.0011311. URL https://doi.org/10.1063/5.0011311.

[30] B. An, J. M. Bergada, and F. Mellibovsky. The lid-driven right-angled isosceles triangular cavity flow. *J. Fluid Mech.*, 875:476–519, 2019. doi: 10.1017/jfm.2019.512.

19